DeCarbon 1 (2023) 100004

Contents lists available at ScienceDirect

DeCarbon

journal homepage: www.sciencedirect.com/journal/decarbon

Research Article

# Binary hole transport layer enables stable perovskite solar cells with PCE exceeding 24%

Xiao Chen [a,1], Bing Guo [a,*,1], Zeyu Zhang [b,**], Bo Zhang [a], Xinzhi Zu [c], Nabonswende Aida Nadege Ouedraogo [d], Jiyeon Oh [e], Yongjoon Cho [e], George Omololu Odunmbaku [a,f], Kun Chen [a,g], Yongli Zhou [a], Shanshan Chen [d], Changduk Yang [e], Juan Du [b,c,***], Kuan Sun [a,****]

[a] MOE Key Laboratory of Low-grade Energy Utilization Technologies and Systems, School of Energy & Power Engineering, Chongqing University, Chongqing 400044, China
[b] School of Physics and Optoelectronic Engineering, Hangzhou Institute for Advanced Study, University of Chinese Academy of Sciences, Hangzhou 310024, China
[c] State Key Laboratory of High Field Laser Physics and CAS Center for Excellence in Ultra-intense Laser Science, Shanghai Institute of Optics and Fine Mechanics (SIOM), Chinese Academy of Sciences (CAS), Shanghai 201800, China
[d] State Key Laboratory of Power Transmission Equipment & System Security and New Technology, School of Energy & Power Engineering, Chongqing University, Chongqing 400044, China
[e] School of Energy and Chemical Engineering, Perovtronics Research Center, Low Dimensional Carbon Materials Center, Ulsan National Institute of Science and Technology (UNIST), 50 UNIST-gil, Ulju-gun, Ulsan 44919, South Korea
[f] CTF Solar, Zur Wetterwarte50, Haus 303, Dresden 01109, Germany
[g] R&D Center, JA Solar Holdings Co., Ltd., Yangzhou 225131, China

ARTICLE INFO

*Keywords:*
Perovskite solar cells
Hole transport materials
Morphology
Polymer
Moisture stability

ABSTRACT

Hygroscopic dopant in hole transport layer (HTL) is a key factor contributing to moisture-induced perovskite degradation and the resulting performance loss over time. This poses obstacles to the commercialization of perovskite solar cells (PSCs). Herein, we mixed two popular hole transport materials, i.e., [2,2′,7,7′-tetrakis(N,N-di-p-methoxyphenyl-amine)9,9′-spirobifluorene] (Spiro-OMeTAD) and poly (3-hexylthiophene-2,5-diyl) (P3HT), to form a binary mixed HTL. Due to the presence of hydrophobic P3HT component, the mixed HTL exhibits improved moisture resistance. In addition, P3HT demonstrates a great ability to interact with the dopants, which changes π-π packing orientation of P3HT from edge-on to face-on and improves its crystallinity, thus increasing hole mobility and hole extraction capability of the mixed HTL. As a result, PSCs equipped with the Spiro-OMeTAD/P3HT mixed HTL exhibit a champion power conversion efficiency (PCE) up to 24.3% and superior operational stability. The cells without encapsulation can maintain 90% initial efficiency after storage in dark ambient conditions (30% RH) for 1200 h. These results suggest that constructing Spiro-OMeTAD/P3HT mixed HTL is a promising strategy to meet the future photovoltaic applications demands with low-cost as well as excellent efficiency and device stability.

## 1. Introduction

Benefiting from its superb opto-electronic properties [1,2], hybrid organic-inorganic perovskite solar cells (PSCs) have become one of the most promising photovoltaic technologies. The power conversion efficiency (PCE) of single-junction PSCs has soared from 3.8% [3] to over 25% [4] in just a few years. High-efficiency PSCs usually possess a classical sandwich structure composed of a perovskite (PVK) light absorber film between electron transport layers (ETLs) and hole transport layers (HTLs). These transport layers are essential for charge extraction and protection from the moisture, thermal and light sensitive perovskite film [5]. As one of the most famous HTLs used in n-i-p PSCs, organic

* Corresponding author.
** Corresponding author.
*** Corresponding author.
**** Corresponding author.
*E-mail addresses:* bing.guo@cqu.edu.cn (B. Guo), zhangzeyu@ucas.ac.cn (Z. Zhang), dujuan@siom.ac.cn (J. Du), kuan.sun@cqu.edu.cn (K. Sun).
[1] These authors contributed equally to this work.

https://doi.org/10.1016/j.decarb.2023.100004
Received 29 January 2023; Received in revised form 5 April 2023; Accepted 12 April 2023
Available online 14 April 2023

molecule 2,2′,7,7′-tetrakis(N,N-di-pmethoxyphenylamine)-9,9′-spirobifluorene (Spiro-OMeTAD) paired with additives bis(trifluoromethane) sulfonimide lithium salt (Li-TFSI) and 4-tert-butylpyridine (tBP) shows suitable energy level alignment with the perovskite absorber, as well as excellent hole transport and extraction capability [6,7]. However, these dopants have been reported to impair device stability because of the hygroscopic nature and dopant-induced ion migration [8], which promotes perovskites degradation [9]. Thus, several strategies on HTL are explored to improve the stability while maintaining high efficiency, e.g. developing new doping strategies [10] or using alternative dopants [11]. Gradated mixed hole transport material is also reported to improve the stability, while the device efficiency is relatively low [12]. In addition, new HTL materials [13] or dopant-free materials [14] have been explored to obtain operationally stable PSCs. Furthermore, interfacial engineering [15–17] is also a promising strategy to reduce interfacial defects, control perovskite crystallization and hinder the perovskite degradation. Despite all the efforts, a facile and cost-effective method that is conducive to the future commercialization of PSCs is yet to be demonstrated.

Herein, we incorporated low-cost, thermally stable and strongly hydrophobic poly(3-hexylthiophene) (P3HT) [18] into Spiro-OMeTAD to form a mixed binary HTL system. Thanks to the hydrophobicity of P3HT, the mixed HTL (m-HTL) can better serve as a protective layer to enhance the long-term stability. In addition, in the presence of Li-TFSI, P3HT not only exhibits a higher degree of molecular order but also shows a preferential "face-on" orientation, i.e., the P3HT molecules are parallel to the substrate, which has significant positive effects on the opto-electronic properties and charge carrier mobility [19]. As a result, PSCs equipped with the Spiro-OMeTAD/P3HT mixed HTL exhibit a champion PCE of 24.3%. Furthermore, the cells without encapsulation can maintain 90% of its initial efficiency after storage in dark ambient conditions (30% RH) for 1200 h. These results indicate that Spiro-OMeTAD/P3HT mixed HTL is a solution to obtain low-cost perovskite solar cells with excellent efficiency and device stability.

## 2. Experimental

### 2.1. Materials

The colloidal $SnO_2$ (15 wt%) was obtained from Alfa Aesar. N, N-dimethylformamide (DMF), and dimethyl sulfoxide (DMSO) were purchased from Sigma-Aldrich. Lead iodide ($PbI_2$) (99.999%), formamidinium iodide (FAI) (99.5%), methylammonium iodide (MAI) (99.9%), methylammonium chloride (MACl) (99.5%), poly(3-hexylthiophene) (P3HT), lithium bis (trifluoromethanesulphonyl) imide (Li-TFSI) and 2,2′,7,7′-tetrakis (N, N di-p-methoxyphenylamine)-9,9′-spirobifluorene (Spiro-OMeTAD) (99.86%) were purchased from You Xuan, Liaoning. 4-tert-butylpyridine (tBP) and phenethylammonium iodide (PEAI) were purchased from Xi'an Polymer Light Technology in China.

### 2.2. Device preparation

The indium tin oxide (ITO) glasses were cleaned by sequentially washing with detergent, deionized (DI) water, acetone and isopropanol (IPA) then treated with UV-ozone for 30 min before use. A thin layer of $SnO_2$ nanoparticle film (2.67 wt% in ammonium hydroxide) was spin coated on the treated ITO substrate at 4000 rpm for 30 s, then annealed in ambient condition at 150 °C for 30 min. The precursor $PbI_2$ (692 mg, 1.5 mmol $mL^{-1}$) in DMF: DMSO (9:1) solution was spin coated onto the cooled substrate at 1500 rpm for 25 s and 2500 rpm for 10 s, and then annealed at 60 °C for 2.5 min. After the $PbI_2$ film cooled down to room temperature, 60 μL of the organic mixture solution of FAI: MAI: MACl (92.4: 6.5: 9.5 mg in 1 mL IPA) was spin coated onto the $PbI_2$ during spinning at 2500 rpm for 3 s, 1350 rpm for 15 s and then 1700 rpm for 12 s. When the resulting film turned from orange to dark brown in glove box, they were thermally annealed at 150 °C for 15 min under ambient conditions. Upon cooling to room temperature, the PEAI (4 mg $mL^{-1}$ in IPA) was spin coated on the perovskite at 5000 rpm for 30 s without annealing. 15 mg P3HT was dissolved in 1 mL of chlorobenzene and stirred for 2 h before use. The Spiro-OMeTAD solution, which consisted of 72.3 mg Spiro-OMeTAD, 35 μL bis(trifluoromethane) sulfonimide lithium salt (Li-TFSI) stock solution (260 mg Li-TFSI in 1 mL acetonitrile), 30 μL 4-tertbutylpyridine (tBP) and 1 mL chlorobenzene, was deposited on top of the perovskite layer at 3000 rpm for 30 s as the control hole transport layer. In addition, different ratios of P3HT solution were added to Spiro-OMeTAD solution and stirred for 0.5 h, then was deposited on top of the perovskite layer at 4000 rpm for 30 s as the mixed hole transport layer. Finally, 7 nm $MoO_3$ and 125 nm Ag films were deposited via thermal evaporation as a counter electrode using a shadow mask.

### 2.3. Device characterization

Photocurrent density-voltage (*J-V*) curves were measured using a solar simulator equipped with 450 W Xenon lamp (Newport 6279 NS) and a Keithley 2400 source meter. The effective active area of the device was defined to be 0.08 $cm^2$ (calibrated mask). *J-V* curves were measured from 1.2 V to −0.1 V (reverse scan, RS) with a scan rate of 100 mV $s^{-1}$. Light intensity was adjusted to AM 1.5G one Sun (100 mW $cm^{-2}$) with a NIM calibrated standard Si solar cell. The incident photon-to-electron conversion efficiency (IPCE) measurement was conducted on an IPCE measurement system. X-ray diffraction (XRD) patterns were acquired using a PANalytical Empyrean diffractometer equipped with Cu Kα radiation (λ = 1.5406 Å). The light pulse was 10 ns. Atomic force microscope (AFM) measurements were conducted on a Dimension Edge (Bruker) by using in tapping mode. Absorption spectra was measured using a Shimadzu UV-1800 UV–vis spectrophotometer. A Fluorescence spectrophotometer (Cary Eclipse, Agilent) with an excitation wavelength of 532 nm was used to collect steady state photoluminescence (PL) spectra. The grazing-incidence wide-angle X-ray scattering (GIWAXS) measurements were carried out at PLS-II 9A beamline of the Pohang Accelerator Laboratory in Korea. The samples were prepared on Si substrates using the identical conditions with the device fabrication. Raman spectra of P3HT were obtained using a high-resolution dispersive Raman microscope (LabRAM HR Evolution, Horiba) under 523 nm excitation wavelength at room temperature. Contact angle was measured with a KRÜSS DSA-100 contact angle measurement instrument. The hole mobility was measured by the space charge limited current (SCLC) method with a configuration of ITO/PEDOT:PSS/HTL/Ag as hole only devices. When operating in the space charge limited current (SCLC) regime, the dark current of the hole only device is described by the Mott–Gurney law:

$$J = 9\varepsilon_0\varepsilon_r\mu V^2/8L^3 \quad (1)$$

where J is the measured current density, L is the film thickness, μ is the hole mobility, $\varepsilon_0$ is the permittivity of vacuum, $\varepsilon_r$ is the relative dielectric constant (assumed to be 3), V is the applied bias. Electrochemical impedance spectroscopy (EIS) and Mott-Schottky measurements (100 Hz) are performed on Chenhua electrochemical workstation (CHI 760E) under conditions. For THz emission device, the spectrometer was driven by a Ti: sapphire laser amplifier (Spectra-Physics® Solstice™ Ace™), which generated 35 fs duration of 800 nm light at 1 kHz repetition rate. The femtosecond laser is split into three beams, one of which is used to excite the ZnTe crystal (1 mm thick, (110)-oriented) to generate THz. The second laser beam is used as the probe light to detect the THz signal of the sample. And the third beam is wavelength-tuned through optical parametric amplification (OPA) as pump light. These three laser beams use two delay lines (TD1、TD2) to adjust the time interval between each other. The electro-optical effect of ZnTe was used to detect THz signal.

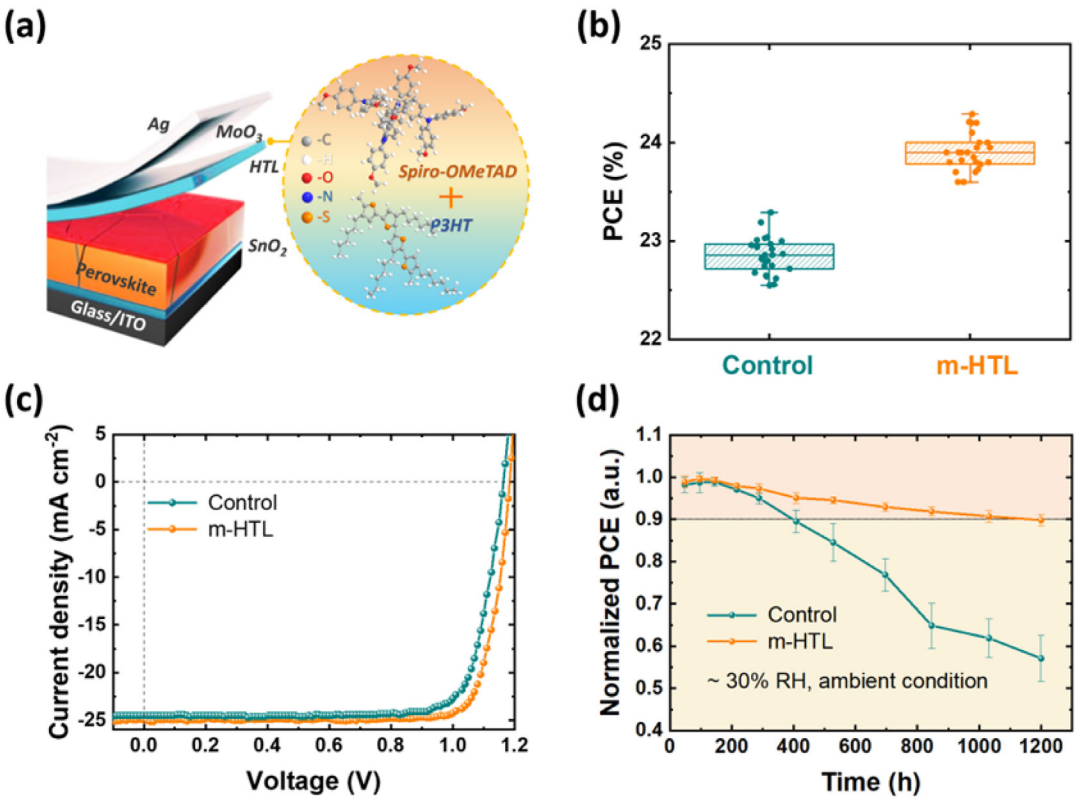


**Fig. 1.** (a) Schematic illustration of the planar structure of n-i-p perovskite solar cell and the chemical structure of Spiro-OMeTAD and P3HT. (b) Statistical distribution of PCE values for control PSCs and m-HTL based PSCs (25 devices are made for each condition). (c) *J-V* curves under reverse scan for the control and m-HTL based devices. (d) PCE evolution of the unencapsulated control and m-HTL based devices (20 devices for each condition) under dark ambient conditions (30% RH).

## 3. Results and discussion

Fig. 1a illustrates the n-i-p cell structure adopted in this work. The top HTL is a mixture of Spiro-OMeTAD and P3HT, labelled as m-HTL. Compared with control cells with only Spiro-OMeTAD as HTL, m-HTL can lead to improved efficiency with good repeatability (Fig. 1b and Fig. S1). The m-HTL based PSCs show a champion PCE of 24.3% (certified 24.22% as shown in Fig. S2), with an open-circuit voltage ($V_{oc}$) of

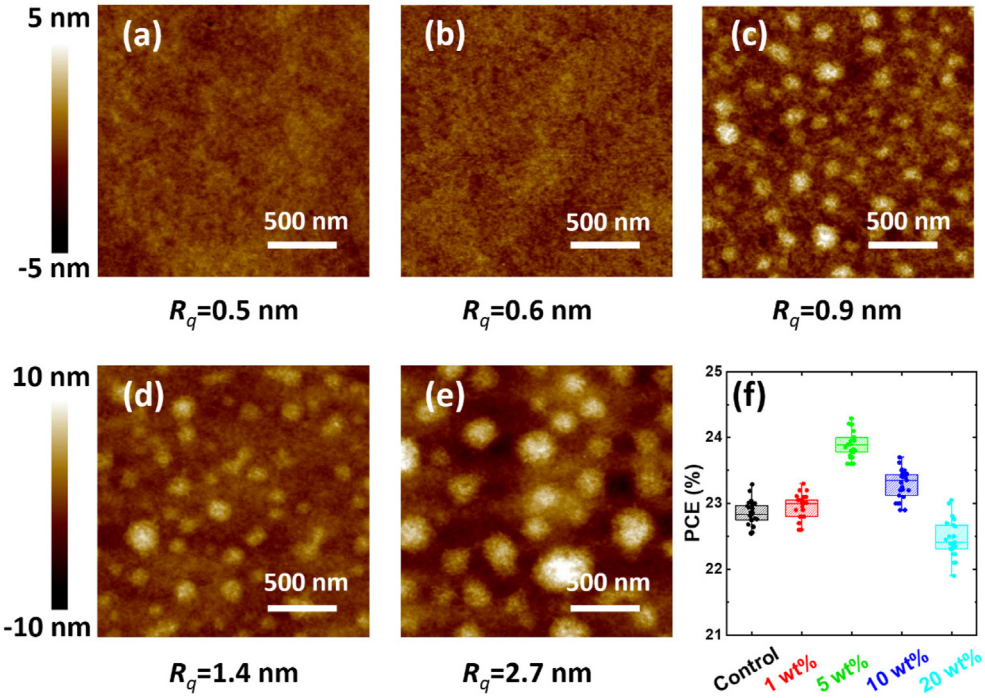


**Fig. 2.** AFM height images in 2*2 μm area of HTLs with different ratios of P3HT: (a) Control Spiro-OMeTAD, (b) 1 wt%, (c) 5 wt%, (d) 10 wt% and (e) 20 wt% P3HT/Spiro-OMeTAD m-HTL. (f) Statistical PCE distribution of PSCs devices with various ratios of P3HT in Spiro-OMeTAD (25 devices are made for each condition).

1.18 V, a short-circuit current density ($J_{sc}$) of 24.94 mA $cm^{-2}$ and a fill factor (FF) of 82.51% (Fig. 1c). The integrated $J_{sc}$ value from the incident photon-to-electron conversion efficiency (IPCE) spectra is 24.35 mA $cm^{-2}$ for the m-HTL based PSC (Fig. S3), which is in good agreement with the $J_{sc}$ value obtained from *J-V* measurements. It is worth mentioning that the PSCs equipped with m-HTL also exhibit excellent long-term stability. They can maintain 90% of its initial efficiency after 1200 h of storage in dark ambient environment (30% RH); while under the same conditions, the average PCE drops below 60% of initial value for the control cells (Fig. 1d).

Firstly, atomic force microscopy (AFM) measurements were employed to monitor the morphology change of the Spiro-OMeTAD film as a function of P3HT concentration (from 1 wt% to 20 wt% P3HT in Spiro-OMeTAD). Fig. 2a–e clearly indicate that phase separation of the binary mixed films becomes clearer with increasing proportion of P3HT within the m-HTL film. In addition, the root-mean-square roughness ($R_q$) of the films shows an upward trend with increasing P3HT content from 0.5 nm to 2.7 nm. Such increased film roughness may hinder carrier extraction across the perovskite/HTL interface, thus the P3HT content requires optimization. Therefore, we fabricated a series of PSCs (active area of 0.08 $cm^2$) based on the following planar structure: glass/indium tin oxide (ITO)/tin oxide ($SnO_2$)/perovskite/phenethylammonium iodide (PEAI)/HTL/molybdenum trioxide ($MoO_3$)/Ag, where the guest P3HT in the HTL was varied. Fig. 2f presents the statistical distribution of PCEs extracted from the fabricated devices as a function of P3HT content, while the corresponding average photovoltaic parameters are listed in Table S1. These results suggest that 5 wt% mixed HTL yields the highest efficiency as a result of improved short-circuit current density, fill factor and relatively low $R_q$ roughness. To gain a deeper understanding of the observed improvements, we conducted further detailed analyses of the

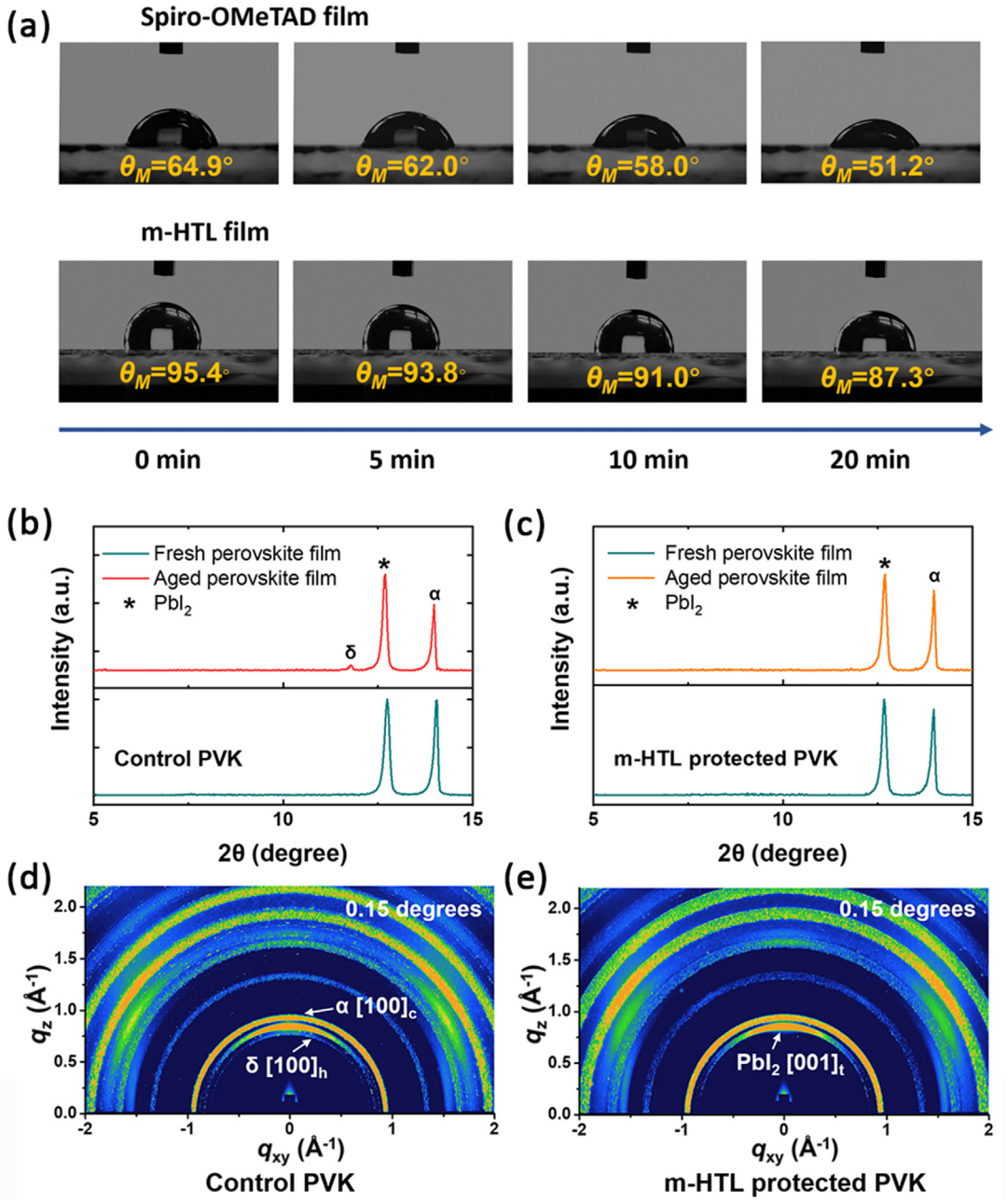


**Fig. 3.** Moisture resistance and suppressed perovskite degradation via m-HTL. (a) Contact angle images as a function of time for the control HTL and m-HTL using deionized water. XRD patterns of fresh and aged perovskite films based on (b) control HTL and (c) m-HTL. 2D GIWAXS patterns of aged perovskite films based on (d) control HTL and (e) m-HTL.

mixed HTL at this fixed ratio.

As an indicator of moisture resistance, water contact-angle measurements tracked in real-time were carried out on HTL with and without P3HT, as shown in Fig. 3a. The initial water contact angle of the m-HTL (95.4°) is much larger than that of the hydrophilic Spiro-OMeTAD film (64.9°), and it remains so at all measurement time considered. In addition, the average rate of change in the measured contact angle as a function of time in the m-HTL is relatively slow, indicating suppressed wettability relative to the control-HTL. The increased contact angle can be attributed the relatively low surface energy surface [20] of P3HT. In general, materials with different surface energies can form segregated phases due to strong repulsive interactions [21], and the component with lower surface energy is preferentially distributed near the surface. Thus, P3HT acts as a barrier against water ingress, and the resulting m-HTL should enhance the operational stability of humidity-sensitive PSCs.

To further confirm the superior moisture resistance of the m-HTL, X-ray diffraction (XRD) measurements were performed on fresh and aged films (the HTL was removed with chlorobenzene prior to the test), as shown in Fig. 3b and c. The control device exhibited a clear degradation of the $FAPbI_3$ perovskite XRD peaks along with the appearance of yellow δ-$FAPbI_3$ phase in the aged diffraction pattern [22]. Meanwhile, no apparent peaks corresponding to the δ-$FAPbI_3$ phase were observed in the diffraction patterns of both fresh and aged perovskite films based on m-HTL even after 200 h. In addition, grazing incidence wide angle X-ray scattering (GIWAXS) on aged films, and UV–vis absorption measurements on both fresh and aged films (Fig. S4) were carried out to confirm these observations (the HTL was removed with chlorobenzene prior to the test). According to the GIWAXS 2D patterns of the aged films (Fig. 3d and e), both perovskite film samples contain two components: trigonal $PbI_2$ and cubic α-$FAPbI_3$ phase $[100]_c$. However, an additional orthorhombic δ-$FAPbI_3$ phase$[100]_h$ [23] was identified in aged control samples (Fig. 3d), whereas this phase was absent in m-HTL based samples (Fig. 3e). The presence of photo-inactive [24] δ-$FAPbI_3$ phase in the aged perovskite film based on control HTL indicates poorer bulk photoelectric properties of the absorber layer, ultimately resulting in the degradation of photovoltaic performance. In sum, the results described so far provide unambiguous evidence that the increased hydrophobicity of the m-HTL via P3HT incorporation is an important factor contributing to the enhanced stability of devices against humidity.

Li-TFSI is the most commonly used dopant in Spiro-OMeTAD [25], and its doping effect on P3HT properties has been studied [26]. It is well known that regioregularity or inter-chain order (in the form of π-π molecular stacking) of semiconducting polymeric films such as P3HT has a significant effect on its optoelectronic properties [27]. UV–vis absorption spectroscopy measurements of P3HT on ITO substrates were carried out to investigate the effect of Li-TFSI doping on the degree of molecular ordering within the P3HT films, as shown in Fig. 4a. The absorption spectra of the dopant-free P3HT layer show a broad peak at 510 nm containing two shoulders at 553 and 600 nm. Upon adding Li-TFSI, a clear red shift in P3HT absorption with significantly enhanced vibronic peak intensity at 600 nm was observed. This increase in absorption at longer wavelengths can be ascribed to decreased disorder in P3HT chain packing [28,29].

In addition, Raman spectra were recorded to further investigate the pristine P3HT and Li-TFSI doped P3HT films. A typical Raman spectrum of P3HT excited at 633 nm is shown in Fig. 4b. There are two dominant Raman modes: a symmetric C═C stretch (around 1440 $cm^{-1}$) and a C–C intra-ring stretch (around 1380 $cm^{-1}$) corresponding to the main in-plane ring-skeleton modes of the thiophene units [30]. For comparison, the Raman signal of the C═C mode of doped film is much stronger than

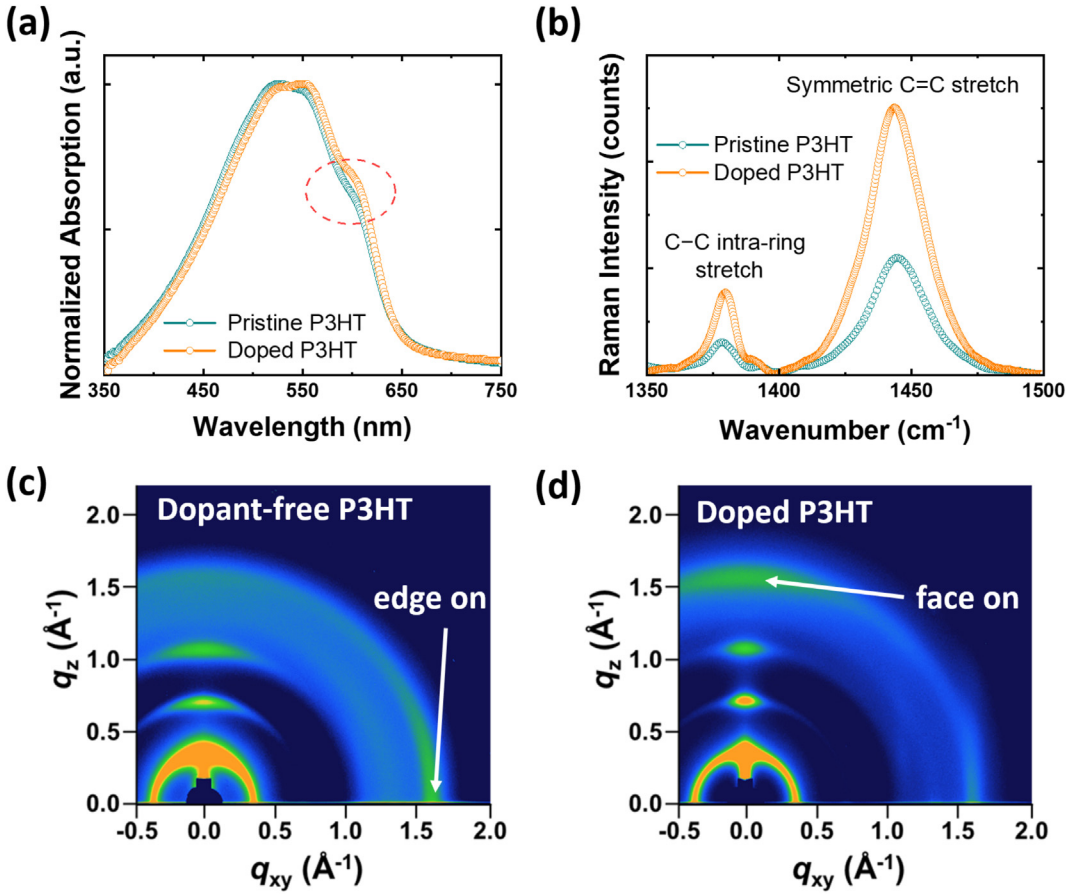


**Fig. 4.** Molecular stacking characterization of m-HTL. (a) Normalized absorption spectra of the P3HT film with or without Li-TFSI, respectively. (b) Raman spectra of the P3HT with or without Li-TFSI, respectively. 2D GIWAXS patterns of the (c) dopant-free P3HT and (d) Li-TFSI doped P3HT films.

that of dopant-free film, which reflects the higher degree of molecular order of P3HT in the Li-TFSI doped P3HT film [31]. The spectra results collectively suggest that the Li-TFSI dopant has a positive effect on either the degree of conjugation of the thiophene chains [32], the degree of inter-chain ordering [26], or a combination of these factors.

In general, the orientation of inter-chain stackings in regioregular P3HT crystallites, namely face-on (π-π stacking direction perpendicular to the substrate) and edge-on (π-π stacking direction parallel to the substrate), can be distinguished from GIWAXS measurements [33]. In Fig. 4c, dopant-free P3HT presents relatively low diffraction peak with indexed (100) and (010) peaks at 0.38 $Å^{-1}$ and 1.64 $Å^{-1}$ corresponding to a lamellar distance $d_1$ of 16.5 Å and π-π stacking distance d of 3.83 Å, which preferentially stacks in an "edge-on" manner. While in the presence of Li-TFSI, the P3HT exhibits higher scattering intensity at out-of-plane direction than that at in-plane direction (Fig. 4d and Fig. S5). This result demonstrates that the dopant breaks the edge-on long-range ordering of P3HT and induces the formation of face-on domains because of the formation of a π-Li chemical bond and reduces the distance between the backbones. As a result, the π-conjugation of the backbones becomes stronger [34]. Furthermore, both the in-plane and out-of-plane (100, 200, 300) diffraction peaks of doped m-HTL significantly increased, which indicated a more ordered structure of the polymer and was consistent with the absorption and Raman spectra [35]. The face-on stacked P3HT domains are beneficial for efficient carrier transfer in vertical structured solar cells because of perpendicular π-π stacking [36,37].

In order to explore whether the orientation of inter-chain stackings of P3HT in m-HTL can still maintain the same trend, we added 2D GIWAXS patterns and Azimuthal integration plots along the (010) plane of P3HT in m-HTL. Firstly, we measured 2D GIWAXS patterns of doped Spiro-OMeTAD to differentiate the face-on π-π stacking was caused by Spiro-OMeTAD or not, as shown in Fig. S6. No π-π stacking signal is observed in either GIWAXS 2D image nor 1D profile for Spiro-OMeTAD. This is mainly due to the amorphous nature of Spiro-OMeTAD, whose spiro-center (a tetrahedral carbon linking two aromatic moieties) prevents crystallization of this organic material [38]. Next, we performed GIWAXS characterization of the dopant-free and doped m-HTL. As shown in Fig. S7 (a) and (b), the diffraction pattern is predominantly from Spiro-OMeTAD. In addition, a weak diffraction ring located at q = 1.64 $Å^{-1}$ is also visible. This is attributed to the π-π stacking of P3HT. To analyze the orientation of the P3HT crystallites, the azimuthal integration plots along the (010) plane (the ring at q = 1.64 $Å^{-1}$) were plotted (Fig. S7c). Compared with the dopant-free m-HTL, the doped m-HTL exhibits a prominent peak ~90°, indicating a face-on π-π stacking of P3HT in m-HTL. It is also worth noting that a new diffraction ring at 0.45 $Å^{-1}$ (the corresponding distances are 14 Å) appears in Fig. S7b. The distance of 14 Å is consistent with the lattice constants a and b obtained from the single crystal structure analysis of Spiro-OMeTAD [39], so this might be a typical diffraction fringe from the Spiro-OMeTAD [40].

Subsequently, space charge limited current (SCLC) measurements for hole mobility determination were carried out to study the effect of preferential face-on stacking in the m-HTL [41]. As shown in Fig. 5a, the hole mobility of m-HTL was derived to be 2.09 × $10^{-4}$ $cm^2$ $V^{-1}$ $s^{-1}$, which is almost twice the value of the control HTL (1.26 × $10^{-4}$ $cm^2$ $V^{-1}$ $s^{-1}$). For comparison, we also measured the hole mobility of a neat P3HT film and a Li-TFSI doped P3HT film. As shown in Fig. S8a, the addition of Li-TFSI also leads to an increase of hole mobility, from 1.15 × $10^{-4}$ $cm^2$ $V^{-1}$ $s^{-1}$ to 2.45 × $10^{-4}$ $cm^2$ $V^{-1}$ $s^{-1}$. Increased hole mobility can facilitate effective hole conduction and alleviate charge recombination at the perovskite/HTL interface [42,43]. We also prepared PSCs using dopant-free/Li-TFSI doped P3HT as HTL. The J-V curves of the dopant-free/doped P3HT based devices are displayed in Fig. S8b. The doped P3HT-based PSCs show a PCE of 16.5% compared to a PCE of 12.9% for dopant-free P3HT devices. The increased photovoltaic parameters, especially FF, indicate that the carrier extraction and hole mobility are promoted. However, the PCE of P3HT-only devices is poor compared to Spiro-OMeTAD PSCs. This is probably due to the higher

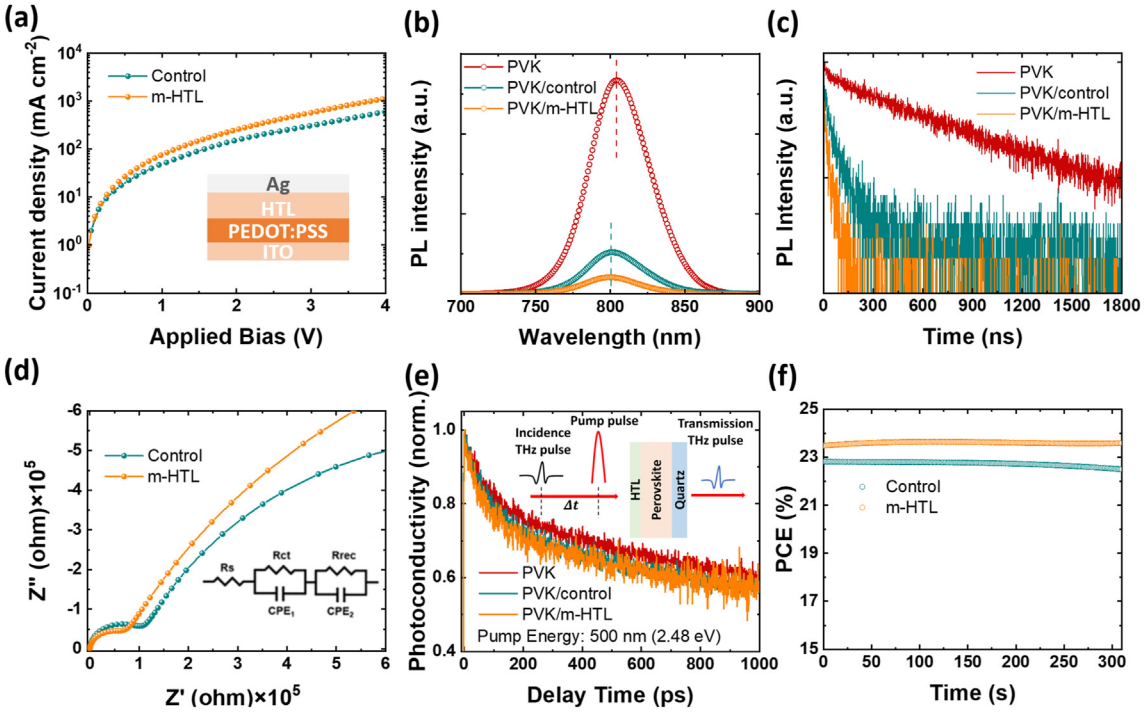


**Fig. 5.** (a) Space-charge-limited current (SCLC) results obtained from the structure of ITO/PEDOT:PSS/HTL/Ag. (b) Steady-state and (c) time-resolved PL spectra of neat perovskite film, perovskite/control (Spiro-OMeTAD) and perovskite/m-HTL. (d) Nyquist plots of the PSCs based on control and m-HTL, the inset in 5d represents the equivalent circuit. (e) Normalized time-resolved THz photoconductivity of neat perovskite film, perovskite/control (Spiro-OMeTAD) and perovskite/m-HTL for 500 nm (2.48 eV) pump with fluences of 35.65 μJ/$cm^2$, the inset in 5e represents the schematic illustration of the TRTS for samples. (f) Steady-state photocurrent for control and m-HTL based devices at the maximum power point under AM 1.5G one Sun illumination.

HOMO energy level and poor physical contact with the perovskite, which may lead to significant $V_{oc}$ loss [31].

Steady-state photoluminescence (PL) measurements (Fig. 5b) were performed to investigate carrier extraction efficiency across the interface. The pristine perovskite film shows an intense PL emission peaked at ~800 nm, while both perovskite/control HTL and perovskite/m-HTL bilayer films exhibited significant PL quenching. Furthermore, the PL peak of PVK/HTLs film is slightly blue-shifted relative to others, which could be related to the reduced defect density in the perovskite film [44–46]. More importantly, the weaker PL emission from the perovskite/m-HTL bilayer film, compared to the perovskite film in contact with the control HTL film, indicates enhanced hole extraction from perovskite to m-HTL [47]. These observations are in agreement with those from time-resolved PL measurements (Fig. 5c and Table S2). The neat perovskite film exhibits an average decay time ($\tau_{avg}$) of 724.1 ns, which significantly decreases to 59.5 and 32.5 ns in the perovskite/control HTL and perovskite/m-HTL bilayer films, respectively. The decreased transient lifetime indicates that the carrier extraction via the m-HTL film is faster than that in the control HTL. Furthermore, the electrochemical impedance spectroscopy (EIS) of control and m-HTL based PSCs further indicates the effective charge transfer as shown in Fig. 5d. Where the first high-frequency arc is assigned to charge transfer resistance ($R_{ct}$) while the second arc at low-frequency represents recombination resistance ($R_{rec}$) at the HTL/perovskite interface [48,49]. Notably, the m-HTL based devices have smaller $R_{ct}$ and larger $R_{rec}$. Fig. S9 shows the Mott–Schottky plots for PSCs employing different HTLs and the m-HTL device had a higher flat-band potential (0.98 V) compared with the control device (0.92 V), indicating that at perovskite/m-HTL interface the carrier extraction is promoted and carrier recombination is inhibited, which could help to improve FF and $V_{oc}$ of the devices. These results described so far therefore provide clear evidence that the presence of Li-TFSI dopants in the m-HTL film induces a higher degree of molecular ordering within P3HT domains and this, in turn, leads to enhanced carrier transport and extraction relative to the control HTL.

To obtain more details on the photoexcited charge carrier relaxation processes from non-equilibrium states on ultrafast time scales after photoexcitation, time-resolved terahertz spectroscopy (TRTS) technique is used. This contact-free and noninvasive method reveals the free and trapped carrier dynamics in the picosecond time scale [50]. The photoconductivity of the carriers in solid curves obeys the relation $\Delta\sigma = Ne^2/\gamma m_e^*$, where N is the charge carrier density, e is the fundamental charge, $\gamma$ is the momentum scattering rate, and $m_e^*$ is the effective mass of charge carriers. For 500 nm (Figs. 5e) and 750 nm (Fig. S10) photoexcitation, all these decay transients are fitted with a single exponential time constant summarized in Table S3. Unlike the trend of time-resolved PL measurements, PVK/control HTL bilayer films showed a relatively small decay compared with neat PVK films in the picosecond time scale, which indicates that the decay mainly arises from the recombination in the bulk PVK films. It is reported that using pure P3HT as HTL could accelerate the recombination of the separated charges in the device compared with Spiro-OMeTAD based device [51]. However, as shown in Fig. 5e, the TRTS data for PVK/control and PVK/m-HTL exhibited almost the same decay curves in the picosecond time scale, which means the recombination in the bulk PVK films did not change even with the addition of P3HT in m-HTL. Therefore, from different time scales, we conclude that P3HT in m-HTL doesn't affect the recombination in the bulk PVK films, but will facilitate carrier extraction and transport relative to the control HTL, leading to enhanced photovoltaic performances.

Finally, to show the impact of HTL on steady-state photovoltaic performance, we monitored the stable PCE output versus time of the control and target devices at the maximum power point under 1 Sun illumination, as shown in Fig. 5f. The control device gave a stabilized PCE output of 22.4% at its $V_{max}$ of 0.99 V, while 23.6% of the stabilized PCE were obtained for the target device at its $V_{max}$ of 1.01 V. The result implies that m-HTL based devices enable better and more stable photovoltaic performance.

## 4. Conclusions

In summary, a successful modification of the conventional Spiro-OMeTAD HTL has been demonstrated by incorporating hydrophobic polymeric P3HT into Spiro-OMeTAD film to improve the efficiency and stability of PSCs. The binary system exhibits excellent hydrophobicity to alleviate the damage caused by hygroscopic dopants. Furthermore, the presence of Li-TFSI dopant shows further positive effects apart from its primary purpose of inducing p-type doping of Spiro-OMeTAD in the m-HTL film. Possible positive effects in the mixed HTL include a higher degree of conjugation within the thiophene chains, as well as inducing "face-on" domains, leading to improved hole extraction and conductivity of the HTL. As a result, the PSCs based on binary mixed HTL system exhibited a champion PCE of 24.3% and significantly improved long-term stability, maintaining 90% of their initial PCE after aging 1200 h in dark ambient conditions without encapsulation. We believe that this strategy will pave the way on the development of low-cost, efficient and stable perovskite solar cells.

## Declaration of competing interest

The authors declare that they have no known competing financial interests or personal relationships that could have appeared to influence the work reported in this paper.

## Acknowledgments

This work was financially supported by research grants from National Key Research and Development Program of China (2022YFB3803300), National Natural Science Foundation of China (62074022 and 52203211), China Postdoctoral Science Foundation (2021M693719), Natural Science Foundation of Chongqing (cstc2020jcyj-msxmX0851), the Youth Talent Support Program of Chongqing (CQYC2021059206 and cstc2021ycjh-bgzxm0334), Chongqing Funds for Distinguished Young Scientists (cstc2021jcyj-jqX0033), Chongqing Postdoctoral Science Foundation (cstc2021jcyj-bshX0203) and Fundamental Research Funds for the Central Universities (2020CDJQY-A055 and 2020CDJ-LHZZ-044).

## Appendix A. Supplementary data

Supplementary data to this article can be found online at https://doi.org/10.1016/j.decarb.2023.100004.

## References

[1] M.A. Green, A. Ho-Baillie, H.J. Snaith, The emergence of perovskite solar cells, Nat. Photonics 8 (2014) 506–514, https://doi.org/10.1038/NPHOTON.2014.134.
[2] Y. Rong, Y. Hu, A. Mei, H. Tan, M.I. Saidaminov, S.I. Seok, M.D. McGehee, E.H. Sargent, H. Han, Challenges for commercializing perovskite solar cells, Science 361 (2018) 1214, https://doi.org/10.1126/science.aat8235.
[3] A. Kojima, K. Teshima, Y. Shirai, T. Miyasaka, Organometal halide perovskites as visible-light sensitizers for photovoltaic cells, J. Am. Chem. Soc. 131 (2009) 6050–6051, https://doi.org/10.1021/ja809598r.
[4] H. Min, D.Y. Lee, J. Kim, G. Kim, K.S. Lee, J. Kim, M.J. Paik, Y.K. Kim, K.S. Kim, M.G. Kim, T.J. Shin, S. Il Seok, Perovskite solar cells with atomically coherent interlayers on $SnO_2$ electrodes, Nature 598 (2021) 444–450, https://doi.org/10.1038/s41586-021-03964-8.
[5] D. Luo, R. Su, W. Zhang, Q. Gong, R. Zhu, Minimizing non-radiative recombination losses in perovskite solar cells, Nat. Rev. Mater. 5 (2019) 44–60, https://doi.org/10.1038/s41578-019-0151-y.
[6] C.Z. Ding, R. Huang, C. Ahlang, J. Lin, L.P. Zhang, D.Y. Zhang, Q. Luo, F.S. Li, R. Osterbacka, C.Q. Ma, Synergetic effects of electrochemical oxidation of Spiro-OMeTAD and Li+ ion migration for improving the performance of n-i-p type perovskite solar cells, J. Mater. Chem. 9 (2021) 7575–7585, https://doi.org/10.1039/d0ta12458c.
[7] S. Wang, M. Sina, P. Parikh, T. Uekert, B. Shahbazian, A. Devaraj, Y.S. Meng, Role of 4-tert-Butylpyridine as a hole transport layer morphological controller in perovskite solar cells, Nano Lett. 16 (2016) 5594–5600, https://doi.org/10.1021/acs.nanolett.6b02158.
[8] S. Wang, Z. Huang, X. Wang, Y. Li, M. Gunther, S. Valenzuela, P. Parikh, A. Cabreros, W. Xiong, Y.S. Meng, Unveiling the role of tBP-LiTFSI complexes in

perovskite solar cells, J. Am. Chem. Soc. 140 (2018) 16720–16730, https://doi.org/10.1021/jacs.8b09809.
[9] K. Liu, Y. Luo, Y. Jin, T. Liu, Y. Liang, L. Yang, P. Song, Z. Liu, C. Tian, L. Xie, Z. Wei, Moisture-triggered fast crystallization enables efficient and stable perovskite solar cells, Nat. Commun. 13 (2022) 4891, https://doi.org/10.1038/s41467-022-32482-y.
[10] J. Kong, Y. Shin, J.A. Rohr, H. Wang, J. Meng, Y. Wu, A. Katzenberg, G. Kim, D.Y. Kim, T.D. Li, E. Chau, F. Antonio, T. Siboonruang, S. Kwon, K. Lee, J.R. Kim, M.A. Modestino, H. Wang, A.D. Taylor, CO2 doping of organic interlayers for perovskite solar cells, Nature 594 (2021) 51–56, https://doi.org/10.1038/s41586-021-03839-y.
[11] S.-M. Bang, S.S. Shin, N.J. Jeon, Y.Y. Kim, G. Kim, T.-Y. Yang, J. Seo, Defect-tolerant sodium-based dopant in charge transport layers for highly efficient and stable perovskite solar cells, ACS Energy Lett. 5 (2020) 1198–1205, https://doi.org/10.1021/acsenergylett.0c00514.
[12] G.W. Kim, G. Kang, M. Malekshahi Byranvand, G.Y. Lee, T. Park, Gradated mixed hole transport layer in a perovskite solar cell: improving moisture stability and efficiency, ACS Appl. Mater. Interfac. 9 (2017) 27720–27726, https://doi.org/10.1021/acsami.7b07071.
[13] M.J. Jeong, K.M. Yeom, S.J. Kim, E.H. Jung, J.H. Noh, Spontaneous interface engineering for dopant-free poly(3-hexylthiophene) perovskite solar cells with efficiency over 24%, Energy Environ. Sci. 14 (2021) 2419–2428, https://doi.org/10.1039/d0ee03312j.
[14] L. Hu, M. Li, K. Yang, Z. Xiong, B. Yang, M. Wang, X. Tang, Z. Zang, X. Liu, B. Li, Z. Xiao, S. Lu, H. Gong, J. Ouyang, K. Sun, PEDOT:PSS monolayers to enhance the hole extraction and stability of perovskite solar cells, J. Mater. Chem. 6 (2018) 16583–16589, https://doi.org/10.1039/c8ta05234d.
[15] Q. Fu, Z. Xu, X. Tang, T. Liu, X. Dong, X. Zhang, N. Zheng, Z. Xie, Y. Liu, Multifunctional two-dimensional conjugated materials for dopant-free perovskite solar cells with efficiency exceeding 22%, ACS Energy Lett. 6 (2021) 1521–1532, https://doi.org/10.1021/acsenergylett.1c00385.
[16] Z. Xiong, X. Chen, B. Zhang, G.O. Odunmbaku, Z.P. Ou, B. Guo, K. Yang, Z.P. Kan, S.R. Lu, S.S. Chen, N.A.N. Ouedraogo, Y. Cho, C. Yang, J.Z. Chen, K. Sun, Simultaneous interfacial modification and crystallization control by biguanide hydrochloride for stable perovskite solar cells with PCE of 24.4%, Adv. Mater. 4 (2022), 2106118 https://doi.org/10.1002/adma.202106118.
[17] G. Yang, Z. Ren, K. Liu, M. Qin, W. Deng, H. Zhang, H. Wang, J. Liang, F. Ye, Q. Liang, H. Yin, Y. Chen, Y. Zhuang, S. Li, B. Gao, J. Wang, T. Shi, X. Wang, X. Lu, H. Wu, J. Hou, D. Lei, S.K. So, Y. Yang, G. Fang, G. Li, Stable and low-photovoltage-loss perovskite solar cells by multifunctional passivation, Nat. Photonics 15 (2021) 681–689, https://doi.org/10.1038/s41566-021-00829-4.
[18] F. De Rossi, G. Renno, B. Taheri, N. Yaghoobi Nia, V. Ilieva, A. Fin, A. Di Carlo, M. Bonomo, C. Barolo, F. Brunetti, Modified P3HT materials as hole transport layers for flexible perovskite solar cells, J. Power Sources 494 (2021), 229735, https://doi.org/10.1016/j.jpowsour.2021.229735.
[19] H. Sirringhaus, P.J. Brown, R.H. Friend, M.M. Nielsen, K. Bechgaard, B.M.W. Langeveld-Voss, A.J.H. Spiering, R.A.J. Janssen, E.W. Meijer, P. Herwig, D.M.d. Leeuw, Two-dimensional charge transport in self-organized, high-mobility conjugated polymers, Nature 401 (1999) 685–688, https://doi.org/10.1038/44359.
[20] Z. Zhang, L. Qu, G. Shi, Fabrication of highly hydrophobic surfaces of conductive polythiophene, J. Mater. Chem. 13 (2003) 2858, https://doi.org/10.1039/b309291g.
[21] Z. Xu, L.-M. Chen, G. Yang, C.-H. Huang, J. Hou, Y. Wu, G. Li, C.-S. Hsu, Y. Yang, Vertical phase separation in poly(3-hexylthiophene): fullerene derivative blends and its advantage for inverted structure solar cells, Adv. Funct. Mater. 19 (2009) 1227–1234, https://doi.org/10.1002/adfm.200801286.
[22] H. Lu, Y. Liu, P. Ahlawat, A. Mishra, W.R. Tress, F.T. Eickemeyer, Y. Yang, F. Fu, Z. Wang, C.E. Avalos, B.I. Carlsen, A. Agarwalla, X. Zhang, X. Li, Y. Zhan, S.M. Zakeeruddin, L. Emsley, U. Rothlisberger, L. Zheng, A. Hagfeldt, M. Gratzel, Vapor-assisted deposition of highly efficient, stable black-phase FAPbI3 perovskite solar cells, Science 370 (2020) 74, https://doi.org/10.1126/science.abb8985.
[23] B.W. Park, N. Kedem, M. Kulbak, D.Y. Lee, W.S. Yang, N.J. Jeon, J. Seo, G. Kim, K.J. Kim, T.J. Shin, G. Hodes, D. Cahen, S.I. Seok, Understanding how excess lead iodide precursor improves halide perovskite solar cell performance, Nat. Commun. 9 (2018) 3301, https://doi.org/10.1038/s41467-018-05583-w.
[24] C.C. Stoumpos, C.D. Malliakas, M.G. Kanatzidis, Semiconducting tin and lead iodide perovskites with organic cations: phase transitions, high mobilities, and near-infrared photoluminescent properties, Inorg. Chem. 52 (2013) 9019–9038, https://doi.org/10.1021/ic401215x.
[25] N.A.N. Ouedraogo, G.O. Odunmbaku, B. Guo, S. Chen, X. Lin, T. Shumilova, K. Sun, Oxidation of spiro-OMeTAD in high-efficiency perovskite solar cells, ACS Appl. Mater. Interfac. 14 (2022) 34303–34327, https://doi.org/10.1021/acsami.2c06163.
[26] D. Mombrú, M. Romero, R. Faccio, Á.W. Mombrú, Unraveling the lithium bis(trifluoromethanesulfonyl)imide (LiTFSI) doping mechanism of regioregular poly(3-hexylthiophene): experimental and theoretical study, J. Phys. Chem. C 124 (2020) 7061–7070, https://doi.org/10.1021/acs.jpcc.0c00407.
[27] W.C. Tsoi, D.T. James, J.S. Kim, P.G. Nicholson, C.E. Murphy, D.D. Bradley, J. Nelson, J.S. Kim, The nature of in-plane skeleton Raman modes of P3HT and their correlation to the degree of molecular order in P3HT:PCBM blend thin films, J. Am. Chem. Soc. 133 (2011) 9834–9843, https://doi.org/10.1021/ja2013104.
[28] P.J. Brown, D.S. Thomas, A. Köhler, J.S. Wilson, J.-S. Kim, C.M. Ramsdale, H. Sirringhaus, R.H. Friend, Effect of interchain interactions on the absorption and emission of poly(3-hexylthiophene), Phys. Rev. B 67 (2003), 064203, https://doi.org/10.1103/PhysRevB.67.064203.
[29] G. Li, V. Shrotriya, J. Huang, Y. Yao, T. Moriarty, K. Emery, Y. Yang, High-efficiency solution processable polymer photovoltaic cells by self-organization of polymer blends, Nat. Mater. 4 (2005) 864–868, https://doi.org/10.1038/nmat1500.
[30] M. Baibarac, M. Lapkowski, A. Pron, S. Lefrant, I. Baltog, SERS spectra of poly(3-hexylthiophene) in oxidized and unoxidized states, J. Raman Spectrosc. 29 (1998) 825–832, https://doi.org/10.1002/(SICI)1097-4555(199809)29:9<825::AID-JRS309>3.3.CO;2-U.
[31] E.H. Jung, N.J. Jeon, E.Y. Park, C.S. Moon, T.J. Shin, T.Y. Yang, J.H. Noh, J. Seo, Efficient, stable and scalable perovskite solar cells using poly(3-hexylthiophene), Nature 567 (2019) 511–515, https://doi.org/10.1038/s41586-019-1036-3.
[32] Y. Gao, J.K. Grey, Resonance chemical imaging of polythiophene/fullerene photovoltaic thin films: mapping morphology-dependent aggregated and unaggregated C=C Species, J. Am. Chem. Soc. 131 (2009) 9654–9662, https://doi.org/10.1021/ja900636z.
[33] P. Muller-Buschbaum, The active layer morphology of organic solar cells probed with grazing incidence scattering techniques, Adv. Mater. 26 (2014) 7692–7709, https://doi.org/10.1002/adma.201304187.
[34] J.W. Jung, J.-S. Park, I.K. Han, Y. Lee, C. Park, W. Kwon, M. Park, Flexible and highly efficient perovskite solar cells with a large active area incorporating cobalt-doped poly(3-hexylthiophene) for enhanced open-circuit voltage, J. Mater. Chem. 5 (2017) 12158–12167, https://doi.org/10.1039/c7ta03541a.
[35] J. Fu, S. Chen, K. Yang, S. Jung, J. Lv, L. Lan, H. Chen, D. Hu, Q. Yang, T. Duan, Z. Kan, C. Yang, K. Sun, S. Lu, Z. Xiao, Y. Li, A "sigma-Hole"-Containing volatile solid additive enabling 16.5% efficiency organic solar cells, iScience 23 (2020), 100965, https://doi.org/10.1016/j.isci.2020.100965.
[36] M.H. Li, J.Y. Shao, Y. Jiang, F.Z. Qiu, S. Wang, J. Zhang, G. Han, J. Tang, F. Wang, Z. Wei, Y. Yi, Y.W. Zhong, J.S. Hu, Electrical loss management by molecularly manipulating dopant-free poly(3-hexylthiophene) towards 16.93 % CsPbI2Br solar cells, Angew. Chem., Int. Ed. Engl. 60 (2021) 16388–16393, https://doi.org/10.1002/anie.202105176.
[37] K. Sun, Z. Xiao, S. Lu, W. Zajaczkowski, W. Pisula, E. Hanssen, J.M. White, R.M. Williamson, J. Subbiah, J. Ouyang, A.B. Holmes, W.W. Wong, D.J. Jones, A molecular nematic liquid crystalline material for high-performance organic photovoltaics, Nat. Commun. 6 (2015) 6013, https://doi.org/10.1038/ncomms7013.
[38] U. Bach, D. Lupo, P. Comte, J.E. Moser, F. Weissörtel, J. Salbeck, H. Spreitzer, M. Grätzel, Solid-state dye-sensitized mesoporous TiO2 solar cells with high photon-to-electron conversion efficiencies, Nature 395 (1998) 583–585, https://doi.org/10.1038/26936.
[39] D. Shi, X. Qin, Y. Li, Y. He, C. Zhong, J. Pan, H. Dong, W. Xu, T. Li, W. Hu, J.L. Bredas, O.M. Bakr, Spiro-OMeTAD single crystals: remarkably enhanced charge-carrier transport via mesoscale ordering, Sci. Adv. 2 (2016), e1501491, https://doi.org/10.1126/sciadv.1501491.
[40] N. Shibayama, H. Maekawa, Y. Nakamura, Y. Haruyama, M. Niibe, S. Ito, Control of molecular orientation of spiro-OMeTAD on substrates, ACS Appl. Mater. Interfac. 12 (2020) 50187–50191, https://doi.org/10.1021/acsami.0c15509.
[41] B. Xu, H. Tian, L. Lin, D. Qian, H. Chen, J. Zhang, N. Vlachopoulos, G. Boschloo, Y. Luo, F. Zhang, A. Hagfeldt, L. Sun, Integrated design of organic hole transport materials for efficient solid-state dye-sensitized solar cells, Adv. Energy Mater. 5 (2015), 1401185, https://doi.org/10.1002/aenm.201401185.
[42] J. Luo, J. Zhu, F. Lin, J. Xia, H. Yang, JinyuYang, R. Wang, J. Yuan, Z. Wan, N. Li, C.J. Brabec, C. Jia, Molecular doping of a hole-transporting material for efficient and stable perovskite solar cells, Chem. Mater. 34 (2022) 1499, https://doi.org/10.1021/acs.chemmater.1c02920.
[43] G.O. Odunmbaku, S.S. Chen, B. Guo, Y.L. Zhou, N.A.N. Ouedraogo, Y.J. Zheng, J. Li, M. Li, K. Sun, Recombination pathways in perovskite solar cells, Adv. Mater. Interfac. 9 (2022), 2102137, https://doi.org/10.1002/admi.202102137.
[44] D.J. Xue, Y. Hou, S.C. Liu, M. Wei, B. Chen, Z. Huang, Z. Li, B. Sun, A.H. Proppe, Y. Dong, M.I. Saidaminov, S.O. Kelley, J.S. Hu, E.H. Sargent, Regulating strain in perovskite thin films through charge-transport layers, Nat. Commun. 11 (2020) 1514, https://doi.org/10.1038/s41467-020-15338-1.
[45] Y. Han, H. Zhao, C. Duan, S. Yang, Z. Yang, Z. Liu, S. Liu, Controlled n-doping in air-stable CsPbI2Br perovskite solar cells with a record efficiency of 16.79, Adv. Funct. Mater. 30 (2020), 1909972, https://doi.org/10.1002/adfm.201909972.
[46] X. Zheng, B. Chen, J. Dai, Y. Fang, Y. Bai, Y. Lin, H. Wei, Xiao C. Zeng, J. Huang, Defect passivation in hybrid perovskite solar cells using quaternary ammonium halide anions and cations, Nat. Energy 2 (2017), 17102, https://doi.org/10.1038/nenergy.2017.102.
[47] Z. Xiong, L. Lan, Y. Wang, C. Lu, S. Qin, S. Chen, L. Zhou, C. Zhu, S. Li, L. Meng, K. Sun, Y. Li, Multifunctional polymer framework modified $SnO_2$ enabling a photostable α-FAPbI3 perovskite solar cell with efficiency exceeding 23%, ACS Energy Lett. 6 (2021) 3824–3830, https://doi.org/10.1021/acsenergylett.1c01763.
[48] J. Chen, X. Zhao, S.G. Kim, N.G. Park, Multifunctional chemical linker imidazoleacetic acid hydrochloride for 21% efficient and stable planar perovskite solar cells, Adv. Mater. 31 (2019), 1902902, https://doi.org/10.1002/adma.201902902.
[49] H. Chen, H. Wang, Y. Xue, Q. Ge, Y. Du, J. Yin, B. Yang, S. Yang, X. Liu, M. Cai, S. Dai, Ultra-high moisture stability perovskite films, soaking in water over 360 min, Chem. Eng. J. 450 (2022), 137033, https://doi.org/10.1016/j.cej.2022.138028.
[50] C. Wang, Z. Zhang, Z. Xiong, X. Yue, B. Zhang, T. Jia, Z. Liu, J. Du, Y. Leng, K. Sun, R. Li, Polaron mobility modulation by bandgap engineering in black phase α-FAPbI3, J. Energy Chem. 76 (2023) 175–180, https://doi.org/10.1016/j.jechem.2022.08.039.
[51] J.C. Brauer, Y.H. Lee, M.K. Nazeeruddin, N. Banerji, Charge transfer dynamics from organometal halide perovskite to polymeric hole transport materials in hybrid solar cells, J. Phys. Chem. Lett. 6 (2015) 3675–3681, https://doi.org/10.1021/acs.jpclett.5b01698.